Electronic transport and contact-free conductance-mapping of polar domains in $SrMnO_3$ films

J. Schaab[1], I. P. Krug[2], H. Doğanay[3], J. Hackl[3], D. M. Gottlob[3], M. I. Khan[3], S. Nemšák[3], L. Maurel[4], E. Langenberg[5], P. A. Algarabel[5], J. A. Pardo[4], C. M. Schneider[3], and D. Meier[1,6]*

[1]*Department of Materials, ETH Zürich, 8093 Zürich, Switzerland*

[2]*Institut für Optik und Atomare Physik, TU Berlin, 10623 Berlin, Germany*

[3]*Peter Grünberg Institute (PGI-6), Forschungszentrum Jülich, 52425 Jülich, Germany*

[4]*Instituto de Nanociencia de Aragón, Universidad de Zaragoza, Mariano Esquillor, 50018 Zaragoza, Spain*

[5]*Instituto de Ciencia de Materials de Argón, Universidad de Zaragoza - CSIC, Pedro Cerbuna 12, 50009 Zaragoza, Spain and*

[6]*Department of Materials Science and Engineering, Norwegian University of Science and Technology, 7491 Trondheim, Norway*

(Dated: March 24, 2016)

Abstract

Conductance mapping with high spatial resolution plays an increasingly important role for the characterization of ferroic domains and their electronic functionality. At present, conductance maps are commonly gained from local two-point measurements, collected in line-by-line scans with a conducting nano-sized probe. Here, we introduce an innovative approach for conductance mapping based on low-energy electron microscopy (LEEM). As a model case we study polar domains of varying conductance in strained $SrMnO_3$. By a direct comparison with conductive atomic force and electrostatic force microscopy, we reveal that the applied LEEM experiment can be considered as an *inverse* $I(V)$-measurement, providing access to the local electronic conductance with nanoscale resolution and short data acquisition times in the order of $10 - 10^2$ milliseconds. Low-energy electrons thus hold yet unexplored application opportunities as minimal-invasive probe for local electronic transport phenomena, opening a promising route towards spatially resolved, high-throughput conductance sampling at the nanoscale.

*dennis.meier@ntnu.no

PACS numbers: 72.20.-i, 84.37.+q, 77.80.Dj

I. INTRODUCTION

Domains in ferroic materials exhibit characteristic transport properties that can be controlled by switching the associated order parameter or, more locally, by inducing minute domain wall movements. Because of the manipulable transport properties such domains offer great application potential enabling, for instance, reversible control of local rectification currents[1] or non-destructive resistive readout of memory devices[2,3]. Additional functionality arises when the domain walls display electronic properties that are different from the surrounding domains[4], including anomalous photovoltaic effects in the presence of conducting walls[5] and the formation of chargeable nano-capacitors separated by insulating walls[6]. To date, such local electronic transport properties are commonly probed by conductive atomic force microscopy (cAFM) in form of local $I(V)$-measurements, i.e. two-point conductance measurements. Due to the applied line-by-line scanning, however, conductance mapping by cAFM is time consuming with data-acquisition times in the order of minutes. In addition, the spatial resolution is ultimately limited by the diameter of the probe tip ($\gtrsim$ 30 nm)[7,8]. A promising but largely unexplored pathway for improving these odds is the application of electron microscopy. The sensitivity to local transport phenomena of scanning electron microscopy (SEM)[9–11] and X-ray photoemission electron microscopy (X-PEEM)[12] has already been shown and first attempts have been made to use these techniques for spatially resolved conductance measurements. A conclusive relation to the local $I(V)$-characteristics, however, has not been verified and due to the irradiation of highly energetic electrons in SEM and photons in X-PEEM unwanted irreversible changes in the electronic surface structure may occur. Thus, fast and non-invasive conductance mapping at the nanoscale is yet to be achieved, gaining even more importance with respect to the future need for adequate monitoring of fabrication processes of envisioned domain- and domain-wall-based nanoelectronics devices.

Here, we demonstrate contact-free nanoscale conductance mapping realized by performing low-energy electron microscopy (LEEM) at variable electron-gun currents. As model a case we investigate strained $SrMnO_3$ because the system exhibits a unique pattern of polar nano-domains of varying electronic conductance but otherwise uniform structural and electrostatic surface properties. This domain configuration allows for studying transport phenomena without interfering contrasts from unknown topography effects or stationary

charges. Based on complementary cAFM and electrostatic force microscopy (EFM) scans we develop a mathematical framework and show that the LEEM experiments on $SrMnO_3$ can be considered as an inverse $I(V)$-measurement: Instead of applying a voltage to the sample, a current I is injected by the electron gun so that a negative voltage V builds up. Since current injection and voltage detection are both realized by the LEEM electron beam, no additional electrical contracts are required. Thus, the current-induced voltage can readily be used for fast conductance mapping with exposure times of a few milliseconds. Analogous to cAFM, our technique probes the electronic conductance normal to the sample surface, while additional in-plane variations become visible due to the lateral resolution. Our results provide novel insight to the electronic conductance of the new functional material $SrMnO_3$ and reveal LEEM as promising tool for fast and non-invasive conductance mapping with nanoscale precision.

II. RESULTS AND DISCUSSION

For our studies, $SrMnO_3$ epitaxial thin films of 20 nm thickness were grown by pulsed laser deposition on (001)-oriented $(LaAlO_3)_{0.3}(Sr_2AlTaO_6)_{0.7}$ (LSAT) substrates with 1.7% tensile strain. Below $T_C = 400$ K the strained films develop a distinct pattern of four domain states with an in-plane polar axis pointing along the $\langle 110 \rangle$ directions of the tetragonal unit cell as detailed elsewhere[6]. Most importantly for our study, $SrMnO_3$ displays well-defined nano-domains of varying conductance at room-temperature. Electronic conductance of the domains has been presented in ref. 6 by cAFM and EFM, but without clarifying the underlying conduction mechanism. Up to date, the electronic conductance has been addressed only at the bulk level in $SrMnO_3$ polycrystals and superlattices[13,14] so that additional information about local phenomena and emergent contact-resistance in cAFM measurements is highly desirable.

A. Electronic transport probed by scanning probe microscopy

We begin our analysis by considering the mechanism responsible for the electronic conductance in our strained $SrMnO_3$ films. Figure 1(a) displays the spatially resolved current distribution measured by cAFM, recorded on a commercial atomic force microscope (NT-

MDT NTEGRA) using Pt-coated silicon tips. Different domains of varying conductance are clearly distinguishable (bright corresponds to high current values), reflecting locally structured conductivity that changes abruptly from one domain to the next. Corresponding $I(V)$-data, evaluated for three different domains, are presented in Fig. 1(b) and their non-linearity indicates non-ohmic behavior. The findings presented in Fig. 1(a) and (b) are in qualitative agreement with literature[6] with the difference that the current values obtained in this work are about two orders of magnitude larger. The latter is indicative of a higher oxygen deficiency, but has no detectable effect on the characteristics of the domain pattern (see Fig. 1(a)).

In order to describe the observed non-ohmic $I(V)$-characteristics in Fig. 1(b) we compared possible transport mechanisms, including thermionic[15–17] and Poole-Frenkel emission[18,19], space-charge-limited conduction[20,21], as well as Fowler-Nordheim tunneling[22]. Best fits were achieved assuming the modified thermionic emission model by Simmons[16], which relates the current I to the electric field $\mathcal{E}$ according to

$$I(\mathcal{E}) = A_{\text{eff}}\, \alpha T^{3/2} (m^*/m_0)^{3/2} \mu \exp(-\frac{\phi_{\text{B}}}{kT}) \mathcal{E} \exp(\beta\sqrt{\mathcal{E}}) \tag{1}$$

Here, A_{eff} is the effective contact area, ϕ_{B} is the potential barrier at the metal-insulator (tip-surface) interface, μ the electron mobility within the bulk, and m^*/m_0 the ratio between the effective and the free mass of the electron ($\alpha = 7.74 \cdot 10^{-4}\,\text{A s}/(\text{cm}^3\,\text{K}^{3/2})$, $\beta = (e/kT)\sqrt{e/(4\pi\epsilon_0\epsilon)}$). The electric field under the AFM probe tip can be written as $\mathcal{E}(V) = V \cdot f(V,\xi)$ with $f(V,\xi)$ accounting for non-linearities in the voltage (e.g. built-in potentials) and the electric-field distribution ξ[8,17,23]. By defining $I_0(T) = I_{00}\, T^{3/2} \exp(-\frac{\phi_{\text{B}}}{kT})$ and $V_0^{-1} = \beta^2 f(V,\xi)$ equation (1) then becomes

$$I(V) = I_0(T) \frac{V}{V_0} \exp(\sqrt{\frac{V}{V_0}}). \tag{2}$$

Corresponding fits (solid lines) are presented together with the measured $I(V)$-data in Fig. 1(b). The agreement between model and experiment holds for all measured temperatures between room-temperature and 315 K (not shown). From the temperature-dependent data an average potential barrier ϕ_B can be derived by plotting $\ln(I_0(T)/T^{3/2})$ as function of $1/T$ (see inset to Fig. 1(b)). The data yield $\phi_{\text{B}} = 0.27 \pm 0.03$ eV and no indication of pronounced domain-dependent variations. Based on ϕ_{B} and the fits in Fig. 1(b) a rough

estimate of the average electron mobility μ at room-temperature can be achieved when assuming a circular tip-surface contact ($A_{\text{eff}} = \pi r_{\text{tip}}^2$, $r_{\text{tip}} = 30$ nm). In addition, an upper limit for the dielectric constant ϵ can be derived assuming a constant electric field over the film ($f(V,\xi) = 1/d_{\text{film}}$, $d_{\text{film}} = 20$ nm). The latter corresponds to a rather drastic but common simplification of the actual electric-field distribution in cAFM[19,24,25]. We note that in our specific case, where the $SrMnO_3$ film thickness is smaller than the radius of the probe tip, this simplification yields an upper limit for $\mathcal{E}$ ($\mathcal{E} \approx V/d_{\text{film}} > V/r_{\text{tip}}$), leading to $\mu \approx (1.4 \pm 0.3) \cdot 10^{-3}$ cm^2/(V s) (for $m^* = m_0$) and $\epsilon \leq 490 \pm 130$. The estimated electron mobility is comparable to perovskite oxides such as $CaMnO_{3-\delta}$ and $Ba_{0.5}Sr_{0.5}TiO_3$ where μ is in the order of 10^{-2} cm^2/(V s) and 10^{-3} cm^2/(V s), respectively[26,27]. The derived upper limit for the dielectric constant ϵ is consistent with frequency-dependent results obtained at low-temperature (ϵ(1 MHz) = 110 at $T = 5$ K)[28]. Based on the excellent agreement between model and data we thus conclude that the electronic conductance in strained $SrMnO_3$ is dominated by the *interface-controlled and bulk-limited*[23,29] transport mechanism described by equations (1) and (2). This implies that the mean-free path of the charge carriers in $SrMnO_3$ is smaller than the thickness of the measured film, i.e., shorter than 20 nm. As a consequence, both the Schottky barrier formed at the tip-surface interface and the mobility of the carriers in the bulk determine the transport behavior[16]. The charge carriers are affected by traps and interface states, which gives rise to additional scattering within the bulk compared to standard Schottky emission[30].

In order to obtain direct evidence for the impact of bulk contributions on the electronic conductance and collect additional information about local variations of the barrier ϕ_{B}, we compared cAFM with complementary EFM measurements as presented in Fig. 1(c) to (e). The EFM maps of mobile (Fig. 1(d)) and fixed (Fig. 1(e)) charges were obtained simultaneously by recording the EFM signals at 2ω and ω, respectively, while scanning in non-contact mode with an AC voltage applied to the tip ($\omega = 41.3$ kHz, $U_{\text{pp}} = 14$ V)[31,32]. The EFM(2ω)-image in Fig. 1(d) shows the same pattern as probed by cAFM (Fig. 1(c)), which proves that the intrinsic bulk properties play a significant role for the domain conductance. The simultaneously recorded EFM(ω)-image in Fig. 1(e) reveals a homogeneous electrostatic surface potential. The latter is in agreement with the in-plane orientation of the polar axis in $SrMnO_3$ and excludes the presence of domain-specific stationary surface charges that may locally alter ϕ_{B}. The EFM data thus corroborate the proposed interface-controlled,

bulk-limited transport mechanism and the material properties derived based on the cAFM experiments.

B. Current-induced potentials visualized by low-energy electron microscopy

After elaborating the electronic transport mechanism in the strained $SrMnO_3$ film in terms of conventional scanning probe microscopy methods, we next discuss the potential of LEEM for conductance mapping. LEEM is a well-established and explicitly powerful method for characterizing, e.g., the surface structure of metals and semiconductors in real-time and with nanoscale resolution ($\gtrsim$ 2 nm)[33]. More recently, LEEM was applied for the analysis and imaging of domains in ferroic oxides[34–36], but the sensitivity of LEEM towards relative, local conductance variations[37,38] has not been explored in detail. In the maybe closest approach, Kautz and coworkers studied the conductivity of in-plane biased graphene based on potentiometry measurements[39]. Their method is particularly strong for measuring variations in the conductance parallel to the surface in electrically conducting materials. In order to expand their approach towards poorly conducting or insulating materials, however, either high in-plane voltages or smaller electrode distances are required both interfering with the imaging by low-energy electrons. Complementary LEEM measurements probing the out-of-plane conductance, that is normal to the sample surface, are virtually non-existing. We thus begin with a direct comparison of spatially resolved LEEM and cAFM data presented in Fig. 2(a) and (b). The LEEM data was recorded under ultrahigh vacuum ($6 \cdot 10^{-10}$ mbar) at the UE56-1 SGM beamline of the *Forschungszentrum Jülich*, BESSY-II storage ring, Helmholtz-Zentrum Berlin using a novel type of aberration-corrected electron microscope (SPECS FE-LEEM P90 AC).

Figure 2(a) and (b) were taken at the same position and demonstrate that standard reflectivity measurements resolve a domain pattern that qualitatively matches with the cAFM conductance map. The LEEM contrast levels, however, are inverted with respect to cAFM, i.e., in the LEEM image conducting domains are darker than insulating domains. This behavior is consistent with band-structure based models relating higher (lower) reflectivity in LEEM to a smaller (larger) number of empty states at the respective kinetic energy[33]. In order to gain more detailed insight, we performed reflectivity measurements with varying kinetic energy of the electrons. The latter was achieved by applying a variable bias voltage

to the sample. The results obtained for bias voltages between −8 V and +12 V at constant electron-gun current $I = 1$ μA are summarized in Fig. 2(c). Figure 2(c) shows the average normalized electron reflectivity evaluated for the four domains marked in the LEEM image in the inset. For all domains a pronounced step-like drop in electron reflectivity is obtained for increasing bias voltage, indicating the so-called MEM-LEEM transition; that is the transition from the mirror-electron-microscopy (MEM) regime of high reflectivity to the energy range where electrons start impinging onto the surface. Since the nature of the energy-dependent change in reflectivity is non-trivial, the voltage $\tilde{V}$ at which the MEM-LEEM transition occurs is often defined based on the point of inflection between maximum and minimum reflectivity[35,40,41].

For the domains highlighted in the inset to Fig. 2(c) the characteristic voltage $\tilde{V}$ shifts by up to ≈ 5 V. Such local shifts in $\tilde{V}$ lead to the strong domain contrasts in LEEM images obtained in the transition region. Typical sources for such shifts in the MEM-LEEM transition are local changes in surface topography, surface potential, or surface polarization, with the latter determining the internal and external screening, band bending, and electron affinity at the surface[33,34,36]. Contributions from the aforementioned sources, however, can be excluded based on our scanning probe microscopy data, which reveal a homogeneous surface topography with a root mean square roughness of only 0.4 ± 0.1 nm (not shown) and no electrostatic contributions as presented in Fig. 1(e). These findings, in addition to the close relation between the cAFM conductance map (Fig. 2(a)) and LEEM reflectivity data (Fig. 2(b)), unambiguously demonstrate that the LEEM contrasts obtained on $SrMnO_3$ originate from potential differences that relate to variations in conductance G.

C. Conductance mapping by low-energy electron microscopy

In order to strengthen our conclusion and elaborate the relation between emergent LEEM contrasts and the local conductance we devised an innovative strategy, performing LEEM experiments as function of the electron-gun current (see Fig. 3). Taking into account that the inelastic mean free path of low-energy electrons in inorganic compounds can reach several nanometers[42], the experiment may be considered as an inverse $I(V)$-measurement complementary to the cAFM data in Fig. 1(b): Instead of applying a voltage to the sample, a current I is injected by the electron gun and a negative voltage is built up at the surface

of the sample due to the finite electronic conductance of $SrMnO_3$. In the LEEM data in Fig. 3(a) the effect is evident from the trend that the MEM-LEEM transition voltage $\tilde{V}$ continuously shifts towards higher values with increasing gun current. As we show in Fig. 3(a) this trend, i.e. the current-induced change in voltage, is captured by the transport model of Simmons (eq. (2)), which enables a quantitative analysis. Since it is the electron-gun current that induces the voltage, however, it is reasonable to use the inverse of equation (2) for analyzing the dose-dependent LEEM experiment

$$V(I) = 4V_0 \times W^2 \left(\frac{1}{2} \sqrt{\frac{I}{I_0(T)}} \right) \tag{3}$$

where W denotes the so-called Lambert-W-function ($z = W(z)e^{W(z)}, z \in \mathbb{C}$). Analogous to the transport measurements in terms of cAFM (see section II A), the electric-field distribution and potential barrier are the only experimental input parameters that require additional assumptions. Obviously, these two parameters are not identical for cAFM and LEEM. Nevertheless, when rigorously applying the same approximation, i.e., $V(I) = \tilde{V}$, $m^* = m_0$, and an average barrier $\phi_\mathrm{B} = 0.27$ eV, we find values for the electron mobility ($\mu = (1.1 \pm 1.0) \cdot 10^{-3}\ \mathrm{cm^2/(V\,s)}$) and dielectric constant ($\epsilon = 80 \pm 8$) that are in reasonable agreement with our transport results (area illuminated by the electron gun: $\mathrm{A_{eff}} = 77 \pm 3\ \mu\mathrm{m}^2$). The agreement between the material constants derived based on cAFM and LEEM justifies the approximation applied for fitting eq. (3) to the LEEM data. Most importantly, the fact that both the cAFM and LEEM results can be described consistently based on the same transport model further strengthens the conclusion that variations in $\tilde{V}$ are a direct measure for changes in conductance ($G := I/\tilde{V}$).

This correlation enables conductance mapping by LEEM as presented in Figs. 3(b) and (c). The conductance maps for 0.1 μA and 2.0 μA in Figs. 3(b) and (c) represent the local conductance normal to the sample surface and were generated based on $\tilde{V}$ values extracted pixel-by-pixel from reflectivity measurements as seen in Fig. 2(c). Figures 3(b) and (c) reflect that the sensitivity of conductance maps increases with increasing electron-gun currents which is consistent with Fig. 3(a). The gain in sensitivity, however, coincides with a loss in spatial resolution because higher gun currents yield more pronounced charging effects that reduce the image quality. In general, the conductance resolution can be optimzed up to the point at which built-up charges prevent arriving electrons from interacting with the sample

and hence cancel the imaging procedure. For the model system $SrMnO_3$ an electron-gun current of 0.1 μA, for instance, allows for resolving conductance variations $\Delta G \approx 30$ nA/V with a spatial resolution $\lesssim 100$ nm.

III. SUMMARY AND CONCLUSION

In summary, by applying cAFM and EFM we demonstrated interface-controlled and bulk-limited transport in strained $SrMnO_3$ and derived estimates for the potential barrier, electron mobility and dielectric constant. We then compared the scanning probe results with LEEM measurements and revealed a correlation between the transport behavior and LEEM reflectivity data. This correlation allows for contact-free imaging of current-induced potential variations, i.e., visualizing areas of different conductance based on low-energy electrons with data acquisition times in the order of a $10 - 10^2$ milliseconds[6]. The applied LEEM reflectivity measurements provide qualitative information with a high spatial resolution that is limited only by the performance of the microscope. Quantitative conductance mapping was realized based on LEEM experiments performed at variable electron-gun current. Emergent contrasts are dominated by the DC bulk conductance normal to the sample surface with in-plane variations becoming visible due to the lateral resolution. The application of dose-dependent LEEM further facilitates non-invasive conductance mapping with adjustable sensitivity / spatial resolution and, most importantly, provides access to local $I(V)$-characteristics. Our concept relies on surface charging which is a well-known and wide-spread effect in electron microscopy, occuring in a large variety of functional materials including, e.g., semiconductors, insulators, ferroelectrics, and silicon-based structures. With this, our results foreshadow possible applications in fundamental materials science, such as time-resolved studies of dynamical transport phenomena, but even beyond the basic research sector. The use of electron beams is already common in industry and even waver-sized samples can be characterized automatically and quickly. Moreover, the usage of a single electron beam for both current injection and non-invasive probing can easily be adapted for industrial purposes. Thus, conductance mapping by low-energy electrons may be employed for industrial sampling and quality monitoring in nanoelectronics fabrication processes.

ACKNOWLEDGMENTS

The authors thank Andres Cano for many enlightening discussions, Martin Lilienblum for technical assistance, and Manfred Fiebig for financial and scientific support. We thank HZB for the allocation of synchrotron beam time and we thankfully acknowledge financial support by HZB. Research at the ETH was financed in part by the SNF (proposal Nr. 200021_149192). L.M., E.L., P.A.A., and J.A.P. acknowledge financial support from Ministerio de Economía y Competitividad under project MAT2014-51982-C2 and Gobierno de Argón under project E26.

---

[1] W. Wu, J. R. Guest, Y. Horibe, S. Park, T. Choi, S.-W. Cheong, and M. Bode, Phys. Rev. Lett. **104**, 217601 (2010).

[2] V. Garcia, S. Fusil, K. Bouzehouane, S. Enouz-Vedrenne, N. D. Mathur, A. Barthélémy, and M. Bibes, Nature **460**, 81 (2009).

[3] A. Gruverman, D. Wu, H. Lu, Y. Wang, H. W. Jang, C. M. Folkman, M. Y. Zhuravlev, D. Felker, M. Rzchowski, C.-B. Eom, and E. Y. Tsymbal, Nano Lett. **9**, 3539 (2009).

[4] D. Meier, J. Phys.: Condens. Matter **27**, 463003 (2015).

[5] S. Y. Yang, J. Seidel, S. J. Byrnes, P. Shafer, C.-H. Yang, M. Rossell, Y.-H. Chu, J. F. Scott, J. W. Ager, III, L. W. Martin, and R. Ramesh, Nature Nanotech. **5**, 143 (2010).

[6] C. Becher, L. Maurel, U. Aschauer, M. Lilienblum, C. Magén, D. Meier, E. Langenberg, M. Trassin, J. Blasco, I. P. Krug, P. A. Algarabel, N. A. Spaldin, J. A. Pardo, and M. Fiebig, Nature Nanotech. **10**, 661 (2015).

[7] B. Cappella and G. Dietler, Surf. Sci. Rep. **34**, 1 (1999).

[8] A. Kumar, T. M. Arruda, A. Tselev, I. N. Ivanov, J. S. Lawton, T. A. Zawodzinski, O. Butyaev, S. Zayats, S. Jesse, and S. V. Kalinin, Sci. Rep. **3**, 1621 (2013).

[9] V. V. Aristov, L. S. Kokhanchik, K.-P. Meyer, and H. Blumtritt, Phys. Status Solidi A **78**, 229 (1983).

[10] V. V. Aristov, L. S. Kokhanchik, and Y. I. Voronovskii, Phys. Status Solidi A **86**, 133 (1984).

[11] J. Li, H. X. Yang, H. F. Tian, C. Ma, S. Zhang, Y. G. Zhao, and J. Q. Li, Appl. Phys. Lett. **100**, 152903 (2012).

[12] J. Schaab, I. P. Krug, F. Nickel, D. M. Gottlob, H. Doğanay, A. Cano, M. Hentschel, Z. Yan, E. Bourret, C. M. Schneider, R. Ramesh, and D. Meier, Appl. Phys. Lett. **104**, 232904 (2014).

[13] C. Chiorescu, J. L. Cohn, and J. J. Neumeier, Phys. Rev. B **76**, 020404 (2007).

[14] S. J. May, T. S. Santos, and A. Bhattacharya, Phys. Rev. B **79**, 115127 (2009).

[15] W. Schottky, Naturwissenschaften **26**, 843 (1938).

[16] J. G. Simmons, Phys. Rev. Lett. **15**, 967 (1965).

[17] S. M. Sze and K. K. Ng, *Physics of Semiconductor Devices* (John Wiley & Sons, Ltd., Hoboken, New Jersey, 2007).

[18] J. Frenkel, Phys. Rev. **54**, 647 (1938).

[19] P. Zubko, D. J. Jung, and J. F. Scott, J. Appl. Phys. **100**, 114113 (2006).

[20] A. Rose, Phys. Rev. **97**, 1538 (1955).

[21] M. A. Lampert and P. Mark, *Current Injection in Solids* (Academic Press, Inc., New York and London, 1970).

[22] R. H. Fowler and L. Nordheim, Proc. R. Soc. A **119**, 173 (1928).

[23] L. Pintilie, I. Vrejoiu, D. Hesse, G. LeRhun, and M. Alexe, Phys. Rev. B **75**, 104103 (2007).

[24] J. Seidel, P. Maksymovych, Y. Batra, A. Katan, S.-Y. Yang, Q. He, A. P. Baddorf, S. V. Kalinin, C.-H. Yang, J.-C. Yang, Y.-H. Chu, E. K. H. Salje, H. Wormeester, M. Salmeron, and R. Ramesh, Phys. Rev. Lett. **105**, 197603 (2010).

[25] J. Guyonnet, I. Gaponenko, S. Gariglio, and P. Paruch, Adv. Mater. **23**, 5377 (2011).

[26] E. Goldyreva, I. Leonidov, M. Patrakeev, and V. Kozhevnikov, J. Solid State Electrochem. **17**, 1449 (2013).

[27] S. Zafar, R. E. Jones, B. Jiang, B. White, V. Kaushik, and S. Gillespie, Appl. Phys. Lett. **73**, 3533 (1998).

[28] H. Sakai, S. Ishiwata, D. Okuyama, A. Nakao, H. Nakao, Y. Murakami, Y. Taguchi, and Y. Tokura, Phys. Rev. B **82**, 180409 (2010).

[29] J. F. Scott, J. Phys.: Condens. Matter **26**, 142202 (2014).

[30] F.-C. Chiu, Advances in Materials Science and Engineering **2014**, 578168 (2014).

[31] F. Johann, A. Hoffmann, and E. Soergel, Phys. Rev. B **81**, 094109 (2010).

[32] P. Girard, Nanotechnology **12**, 485 (2001).

[33] E. Bauer, *Surface Microscopy with Low Energy Electrons* (Springer Science+Business Media New York, 2014).

[34] S. Cherifi, R. Hertel, S. Fusil, H. Béa, K. Bouzehouane, J. Allibe, M. Bibes, and A. Barthélémy, Phys. Status Solidi RRL **4**, 22 (2010).

[35] J. E. Rault, W. Ren, S. Prosandeev, S. Lisenkov, D. Sando, S. Fusil, M. Bibes, A. Barthélémy, L. Bellaiche, and N. Barrett, Phys. Rev. Lett. **109**, 267601 (2012).

[36] N. Barrett, J. E. Rault, J. L. Wang, C. Mathieu, A. Locatelli, T. O. Mentes, M. A. Niño, S. Fusil, M. Bibes, A. Barthélémy, D. Sando, W. Ren, S. Prosandeev, L. Bellaiche, B. Vilquin, A. Petraru, I. P. Krug, and C. M. Schneider, J. Appl. Phys. **113**, 187217 (2013).

[37] L. Mayer, J. Appl. Phys. **26**, 1228 (1955).

[38] K. N. Maffitt, J. Appl. Phys. **39**, 3878 (1968).

[39] J. Kautz, J. Jobst, C. Sorger, R. M. Tromp, H. B. Weber, and S. J. van der Molen, Scientific Reports **5**, 13604 (2015).

[40] R. L. Bihan, J. L. Chartier, and L. Jean, Ferroelectrics **17**, 429 (1977).

[41] I. Krug, N. Barrett, A. Petraru, A. Locatelli, T. O. Mentes, M. A. Nio, K. Rahmanizadeh, G. Bihlmayer, and C. M. Schneider, Applied Physics Letters **97**, 222903 (2010).

[42] S. Tanuma, C. J. Powell, and D. R. Penn, Surf. Interface Anal. **17**, 927 (1991).

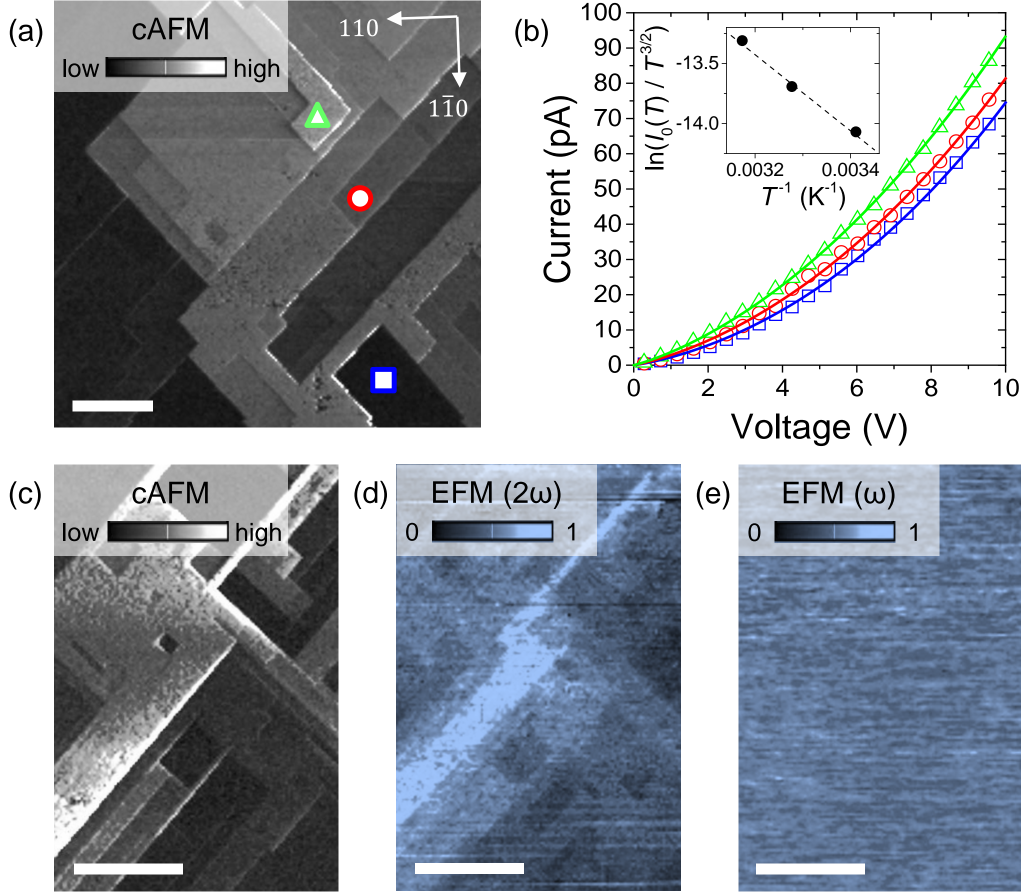

FIG. 1. Transport properties of strained $SrMnO_3$ probed by scanning probe microscopy. (a) cAFM scan obtained with a sample bias of 0.2 V, revealing nano-domains of varying conductance. Scale bar, 2 μm. (b) Local $I(V)$-curves recorded at the spots marked in (a). Solid lines represent fits to the $I(V)$-curves according to equation (2). The inset shows an Arrhenius plot of the temperature-dependent fit constant $I_0(T)$ of equation (2) from measurements on a single domain. (c) cAFM image recorded at a different sample position. Scale bar, 5 μm. (d) Normalized EFM(2ω)-image obtained at the same sample position shown in (c). The EFM scan reveals the spatial distribution of mobile charge carriers, imaged in non-contact mode. Scale bar, 5 μm. (e) Corresponding EFM(ω)-image recorded at the same position as the scans in (c) and (d) reflecting a homogeneous electrostatic surface potential with no indication of domain-related stationary charges. Scale bar, 5 μm.

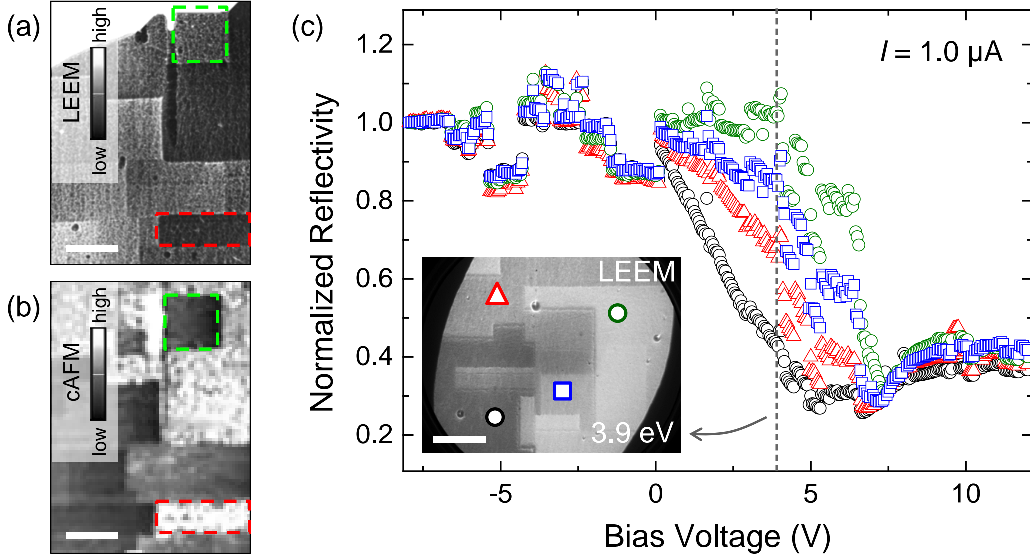

FIG. 2. LEEM reflectivity measurements. (a) and (b) LEEM and cAFM images recorded at the same position. Green and red dashed lines highlight examples for insulating and conductive domains, respectively, which lead to opposite contrasts in LEEM compared to cAFM. The LEEM image in (b) was obtained with an exposure time of 500 ms. A closer inspection of (a) and (b) further reveals differences in the relative contrasts. This is because cAFM resolves variations in current, $\Delta I(V_{\mathrm{const}})$, while LEEM maps differences in the surface potential, $\Delta V(I_{\mathrm{const}})$, which are different due to the nonlinear $I(V)$ characteristic of $SrMnO_3$ (see Fig. 1(b)). Scale bars, 2 μm. (c) MEM-LEEM transition measured with an electron-gun current of 1.0 μA. Different curves correspond to the different domains marked in the inset and, for comparison, were normalized with respect to the reflectivity obtained below -7 eV. The inset shows a LEEM image taken with an exposure time of 250 ms at a bias voltage of 3.9 eV, indicated by the dashed line in (c). Scale bar, 2 μm.

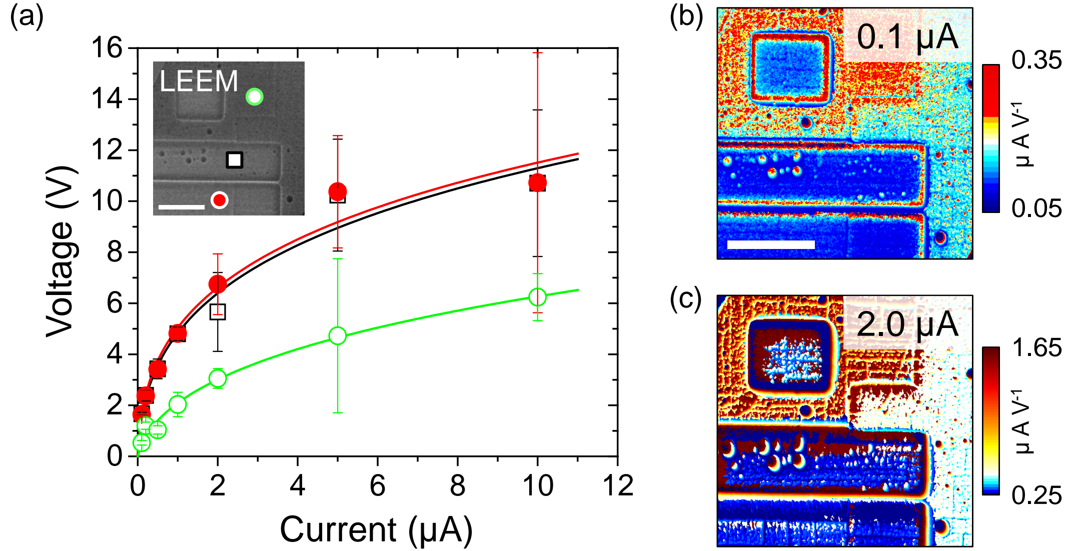

FIG. 3. Current-induced voltage and conductance maps measured by LEEM. (a) Data points present the detected MEM-LEEM transition voltage $\tilde{V}$ as function of the gun current I for the three domains marked in the LEEM image in the inset. The LEEM image was obtained at 1.0 V bias voltage with $I = 1.0\ \mu$A. Scale bar, 2 μm. Each data point is obtained from a series of reflectivity measurements analogous to the data presented in Fig. 2(c). For increasing gun currents the MEM-LEEM transition voltage shifts to higher energies which is captured by fitting the $V(I)$ characteristics described by equation (3) to the LEEM data with $V(0) = 0$ (solid lines). (b) and (c) Conductance maps obtained for gun current of 0.1 μA and 2.0 μA at the position shown in the inset to (a). Colors represent the local conductance G. Scale bar in (b), 2 μm.